Supplementary materials for "Validation of XCO_2 derived from SWIR spectra of GOSAT TANSO-FTS with aircraft measurement data"

Makoto Inoue, Isamu Morino, Osamu Uchino, Yuki Miyamoto, Yukio Yoshida, Tatsuya Yokota, Toshinobu Machida, Yousuke Sawa, Hidekazu Matsueda, Colm Sweeney, Pieter P. Tans, Arlyn E. Andrews, Sebastien C. Biraud, Tomoaki Tanaka, Shuji Kawakami, and Prabir K. Patra

S-1. CAKs with respect to solar zenith angle

Figure S-1 shows examples of CAK for GOSAT XCO_2 at seven different solar zenith angles. It is found that the CAK is a function of solar zenith angle as mentioned in Sect. 3.1.4.

S-2. Comparisons by curve fitting method

As discussed in Sect. 3.2, it was difficult to compare GOSAT XCO_2 with aircraft measurement data at some observation sites where there was a paucity of flight data on the day when GOSAT was scheduled to overpass. However, the temporal interpolation of aircraft-based XCO_2 by a curve fitting method enables temporally matched cases to be obtained for all observation sites of CONTRAIL, NOAA, DOE, and NIES (41 sites). Based on Miyamoto et al. (2013), we attempted to fit aircraft-based XCO_2 with the following equation (S.1) containing annual trend and annual / semiannual sinusoidal variations.

$$XCO_2(t) = Intercept + Trend \times t + \frac{Amp_1}{2} \times \cos\left(2\pi \frac{t-\Phi_1}{12}\right) + \frac{Amp_2}{2} \times \cos\left(4\pi \frac{t-\Phi_2}{12}\right) \quad \text{(S.1)}$$

where $XCO_2(t)$ is the XCO_2 value at time t, $Intercept$ denotes the column abundance on 1 January 2007 without sinusoidal variations, and $Trend$ represents the monthly growth rate, Amp_1 and Amp_2 are sinusoidal variations with periods of one year and a half year, respectively, and Φ_1 and Φ_2 are phases in the annual and semiannual sinusoidal variations, respectively. We converted aircraft-based XCO_2 without CAK after 2007 into an XCO_2 time series (i.e. continuous data) by curve fitting. The GOSAT XCO_2 data observed within the $\pm 2^\circ$ and $\pm 5^\circ$ latitude/longitude boxes centered at each aircraft measurement site were compared with the calculated aircraft-based XCO_2 (i.e. estimates) in the GOSAT overpass time.

Before the validation, we focus on the uncertainties of aircraft-based XCO_2 arisen from the curve fitting. It is considered that there are significant interannual differences of CO_2 uptake during the Northern Hemisphere summer between 2009 and 2010 (e.g. Guerlet et al., 2013). Our estimation does not consider the interannual differences in

the seasonal uptake of CO_2, so this may lead to an error source in this curve fitting approach. In this study, the uncertainties due to the curve fitting method are defined and calculated. We defined 1 σ of the differences between "true aircraft-based XCO_2 values" and "the calculated values (i.e. estimates) in aircraft measurement time of the respective XCO_2 data by curve fitting" as uncertainties due to the curve fitting method. Table S-1 summarizes 1 σ of the differences at each aircraft site. The uncertainties are about or less than 1 ppm, except two sites (SUR and BNE). In addition, Fig. S-2 shows the distance from each aircraft site to the GOSAT data obtained within $\pm 5^\circ$ boxes of each site for all sites (i.e. absolute values of the latitude/longitude differences). We found that the matched data are distributed with uniformity in $\pm 5^\circ$ boxes.

The results of the comparison for the $\pm 2^\circ$ and $\pm 5^\circ$ boxes centered at respective sites are shown in Figs. S-3 to S-16. In addition, the average and 1 σ of the differences between GOSAT SWIR XCO_2 and aircraft-based XCO_2 at each aircraft site using curve fitting are listed in Tables S-2 and S-3 for land and ocean cases, respectively. For many observation sites at mid- and high-latitudes over the Northern Hemisphere, aircraft-based XCO_2 displayed a seasonal amplitude of approximately 7-8 ppm. In contrast, seasonal changes were obscure at Sydney (SYD) over the Southern Hemisphere. The growth rate of aircraft-based XCO_2 was about 2 ppm yr^{-1} at most sites, which corresponded to previous studies of CO_2 variations. In most land regions, the GOSAT SWIR XCO_2 agreed with aircraft-based XCO_2. There were also good correlations between both data sets over several ocean regions and the correlation coefficients were 0.92 and 0.61 with significance at the 99% level over Honolulu (HNL) and Manila (MNL), respectively, for the $\pm 5^\circ$ boxes. Figure S-17 shows the scatter diagrams between GOSAT SWIR XCO_2 and aircraft-based XCO_2 (estimated values at the GOSAT overpass time) obtained by the curve fitting method at all observation sites. In land regions, the correlation coefficients were 0.81 with significance at the 99% level for both $\pm 2^\circ$ and $\pm 5^\circ$ boxes. Over ocean regions, the correlation coefficients were 0.72 and 0.75 with significance at the 99% level for $\pm 2^\circ$ and $\pm 5^\circ$ boxes, respectively. GOSAT data were negatively biased by about 1-2 ppm. These results were consistent with those of the direct comparison by temporally matched cases described in Sect. 4.3 (Table 4).

Thus, the curve fitting method is useful to validate the GOSAT products over all locations.

References

Guerlet, S., Basu, S., Butz, A., Krol, M., Hahne, P., Houweling, S., Hasekamp, O. P., and Aben, I.: Reduced carbon uptake during the 2010 Northern Hemisphere summer from GOSAT, Geophys. Res. Lett., 40, 2378-2383, doi:10.1002/grl.50402, 2013.

Miyamoto, Y., Inoue, M., Morino, I., Uchino, O., Yokota, T., Machida, T., Sawa, Y., Matsueda, H., Sweeney, C., Tans, P. P., Andrews, A. E., Biraud, S. C., and Patra, P. K.: Atmospheric column-averaged mole fractions of carbon dioxide at 53 aircraft measurement sites, Atmos. Chem. Phys., 13, 5265-5275, doi:10.5194/acp-13-5265-2013, 2013.

Table S- 1: The 1 standard deviation (1 σ) of the differences between the aircraft-based XCO_2 values and the fitted values (estimates) of the respective aircraft-based XCO_2 data by curve fitting in observation time.

site	number	1σ [ppm]
(1) AMS	153	0.830
(2) LHR	105	0.839
(3) YVR	224	1.071
(4) CDG	134	1.016
(5) MXP	50	0.889
(6) FCO	44	0.709
(7) ICN	75	1.657
(8) NRT	3086	1.201
(9) HND	179	1.156
(10) NGO	327	1.585
(11) KIX	251	1.145
(12) DEL	149	0.837
(13) TPE	51	0.848
(14) HNL	218	0.593
(15) MNL	41	0.581
(16) BKK	374	0.973
(17) GUM	28	0.311
(18) SIN	343	0.641
(19) CGK	223	0.656
(20) SYD	186	0.556
(21) PFA	76	0.908
(22) BRM	83	0.860
(23) ESP	123	1.097
(24) DND	46	1.220
(25) LEF	99	1.184
(26) NHA	92	0.986
(27) WBI	67	1.161
(28) THD	48	0.773
(29) BNE	63	2.303
(30) CAR	94	0.899
(31) HIL	65	1.210
(32) AAO	240	1.604
(33) CMA	108	1.158
(34) SCA	71	0.930
(35) TGC	69	0.758
(36) RTA	44	0.917
(37) SGP	148	1.248
(38) YAK	11	1.910
(39) SUR	42	3.224
(40) NOV	36	1.099
(41) SGM	41	1.454
All data	7907	1.149

Table S- 2: The average and 1 standard deviation (1 σ) of the differences between GOSAT XCO_2 observed over land region within $\pm 2^\circ$ and $\pm 5^\circ$ latitude/longitude boxes centered at each aircraft site and aircraft-based XCO_2 using curve fitting method.

Land		± 2 deg.			± 5 deg.	
site	number	average [ppm]	1σ [ppm]	number	average [ppm]	1σ [ppm]
(1) AMS	14	0.481	2.262	124	-1.564	2.084
(2) LHR	40	-0.957	2.088	155	-1.112	2.063
(3) YVR	6	0.328	4.117	166	-1.373	2.471
(4) CDG	57	-1.393	1.905	262	-1.373	2.054
(5) MXP	32	0.071	2.501	181	0.444	2.481
(6) FCO	43	-1.301	2.126	195	-2.089	2.346
(7) ICN	66	0.287	2.828	189	-0.254	2.846
(8) NRT	65	-0.461	2.259	105	-0.545	2.471
(9) HND	76	-0.897	2.408	108	-1.040	2.507
(10) NGO	25	-0.459	2.792	120	-0.339	2.442
(11) KIX	18	-0.770	2.507	103	-0.162	2.484
(12) DEL	214	-1.548	1.857	854	-2.153	1.940
(13) TPE	11	0.899	1.712	70	0.559	2.165
(14) HNL	0	-	-	0	-	-
(15) MNL	0	-	-	2	-3.968	0.641
(16) BKK	18	0.215	2.214	77	-0.798	2.391
(17) GUM	0	-	-	0	-	-
(18) SIN	0	-	-	0	-	-
(19) CGK	2	-1.147	0.565	5	-1.561	0.616
(20) SYD	83	-0.740	2.314	370	-1.448	2.067
(21) PFA	37	0.574	1.990	108	-0.653	2.322
(22) BRM	43	-0.018	2.944	286	-0.991	2.810
(23) ESP	0	-	-	84	-0.826	2.529
(24) DND	70	-2.264	1.689	402	-1.483	2.455
(25) LEF	60	-1.623	2.359	299	-1.412	2.641
(26) NHA	23	-1.602	1.431	169	-1.106	2.290
(27) WBI	44	-2.210	2.434	615	-2.246	1.954
(28) THD	80	0.147	2.282	329	-0.746	2.087
(29) BNE	132	-3.014	1.909	765	-3.095	2.295
(30) CAR	161	-3.542	1.678	766	-3.287	2.004
(31) HIL	173	-2.514	1.615	628	-2.416	1.933
(32) AAO	139	-1.122	2.002	621	-1.140	2.073
(33) CMA	45	-0.933	2.417	205	-1.410	2.322
(34) SCA	80	-1.636	1.763	521	-1.548	1.908
(35) TGC	47	-1.491	1.639	546	-1.709	1.705
(36) RTA	0	-	-	0	-	-
(37) SGP	184	-2.809	1.740	835	-2.745	1.926
(38) YAK	50	-1.962	2.303	183	-2.070	2.408
(39) SUR	52	-2.150	2.495	269	-2.752	2.633
(40) NOV	53	-1.250	2.593	323	-1.469	2.823
(41) SGM	70	0.594	2.494	106	0.384	2.575
All data	2313	-1.555	2.364	11146	-1.813	2.373

Table S- 3: The average and 1 standard deviation (1 σ) of the differences between GOSAT XCO_2 observed over ocean region within $\pm 2^\circ$ and $\pm 5^\circ$ latitude/longitude boxes centered at each aircraft site and aircraft-based XCO_2 using curve fitting method.

Ocean		$\pm$2 deg.			$\pm$5 deg.	
site	number	average [ppm]	1σ [ppm]	number	average [ppm]	1σ [ppm]
(1) AMS	0	-	-	0	-	-
(2) LHR	0	-	-	1	-1.712	-
(3) YVR	0	-	-	1	0.699	-
(4) CDG	0	-	-	0	-	-
(5) MXP	1	0.793	-	4	-0.732	1.562
(6) FCO	0	-	-	31	-4.652	2.164
(7) ICN	0	-	-	55	-1.661	3.537
(8) NRT	1	0.455	-	9	-2.952	3.051
(9) HND	1	0.414	-	10	-2.631	2.770
(10) NGO	0	-	-	19	-2.435	4.009
(11) KIX	0	-	-	35	-2.699	3.565
(12) DEL	0	-	-	0	-	-
(13) TPE	19	-0.633	2.704	38	-0.283	2.835
(14) HNL	30	-2.062	1.271	98	-1.639	1.330
(15) MNL	0	-	-	66	-1.857	1.664
(16) BKK	4	-4.054	1.868	11	-3.500	1.505
(17) GUM	1	0.834	-	44	-0.750	-1.454
(18) SIN	1	-1.503	-	4	-2.151	0.772
(19) CGK	3	-1.161	1.361	21	-2.049	1.495
(20) SYD	1	-1.578	-	54	-1.538	1.544
(21) PFA	0	-	-	0	-	-
(22) BRM	0	-	-	0	-	-
(23) ESP	1	0.901	-	1	0.901	-
(24) DND	0	-	-	0	-	-
(25) LEF	0	-	-	0	-	-
(26) NHA	1	-0.927	-	6	-2.934	1.999
(27) WBI	0	-	-	0	-	-
(28) THD	0	-	-	3	-1.172	3.231
(29) BNE	0	-	-	0	-	-
(30) CAR	0	-	-	0	-	-
(31) HIL	0	-	-	0	-	-
(32) AAO	0	-	-	0	-	-
(33) CMA	3	-2.070	1.142	24	-1.094	2.491
(34) SCA	0	-	-	63	-0.959	1.959
(35) TGC	0	-	-	58	-1.501	1.379
(36) RTA	17	-1.939	1.561	45	-2.170	1.280
(37) SGP	0	-	-	0	-	-
(38) YAK	0	-	-	0	-	-
(39) SUR	0	-	-	0	-	-
(40) NOV	0	-	-	0	-	-
(41) SGM	1	3.845	-	7	0.093	3.513
All data	85	-1.524	2.016	708	-1.729	2.349

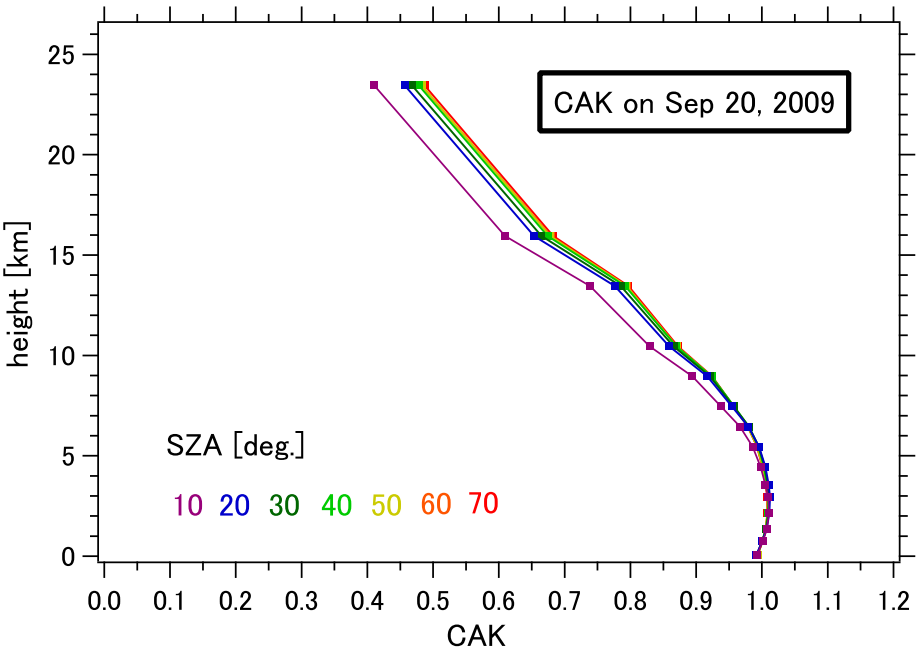

Fig. S- 1: Examples of CAK for GOSAT XCO_2 on 20 September, 2009. The shapes of CAKs at seven different solar zenith angles are shown by color.

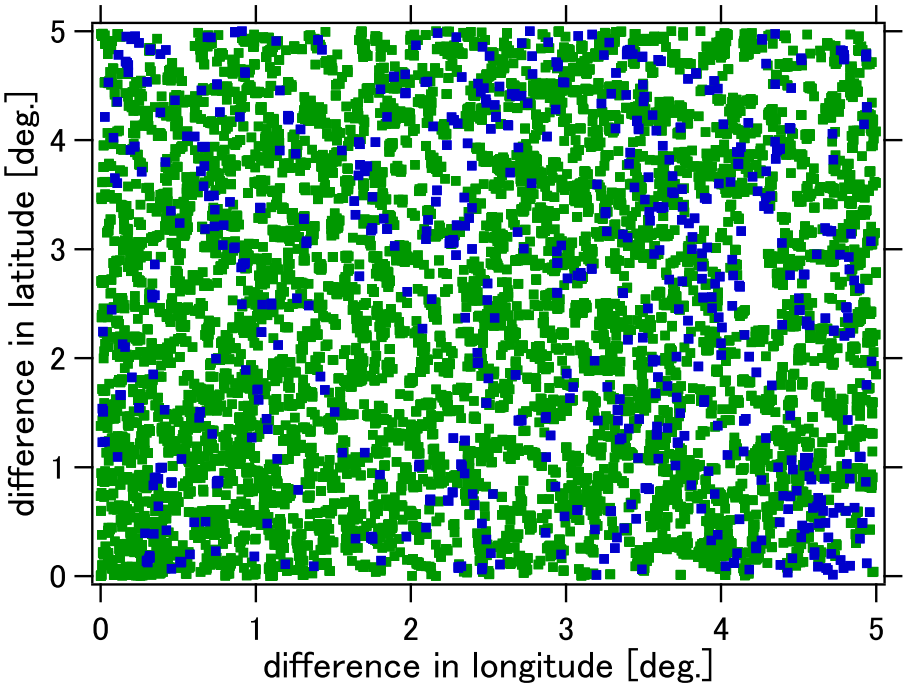

Fig. S- 2: The distance from each aircraft site to the location of GOSAT data obtained within ±5° latitude/longitude boxes of each site (i.e. absolute values of the latitude/longitude differences). Green and blue dots indicate the distance from aircraft site to the location of the GOSAT data retrieved over land and ocean, respectively.

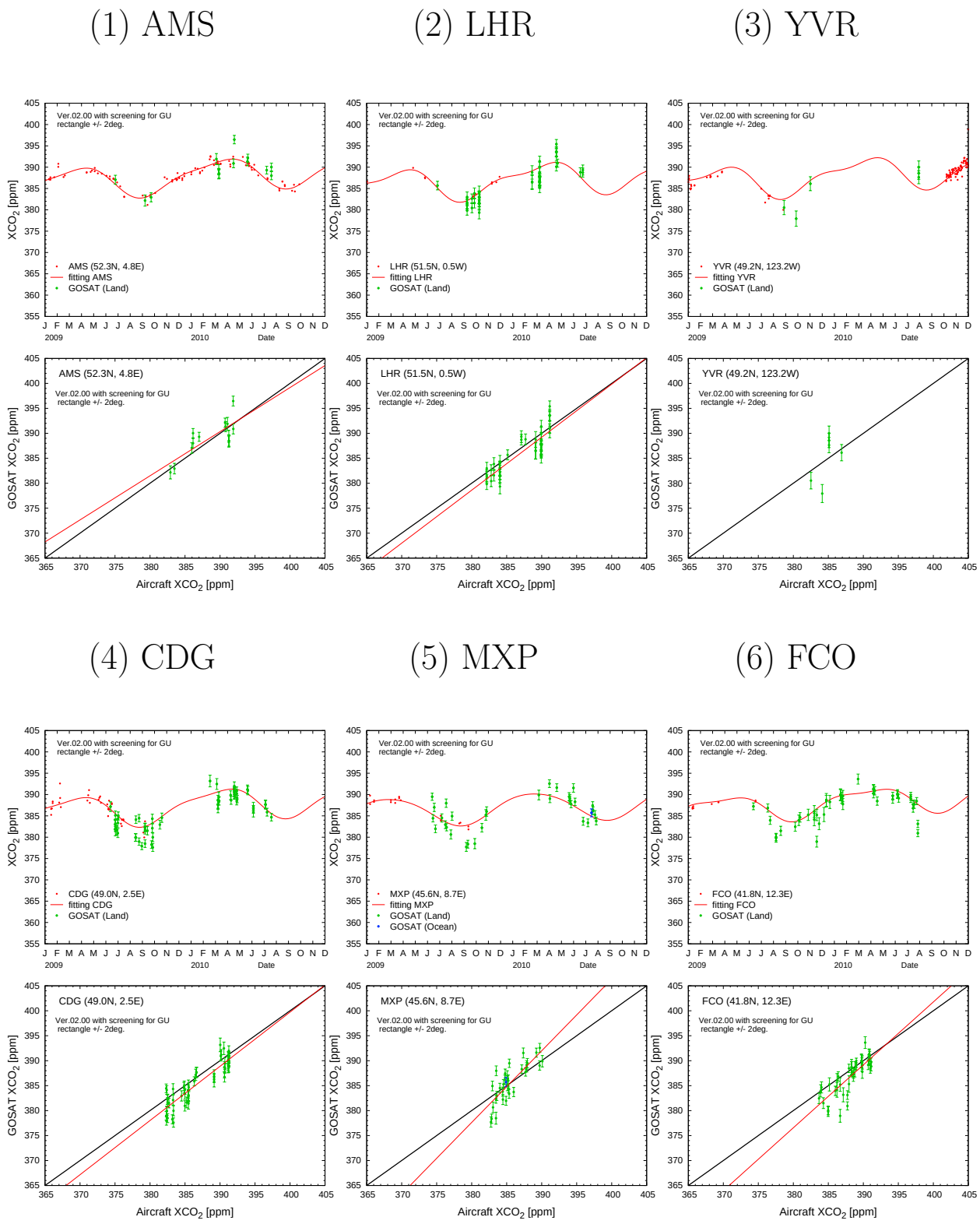

Fig. S- 3: Temporal variations of aircraft-based XCO_2 and GOSAT XCO_2 observed within $\pm 2^\circ$ atitude/longitude boxes centered at each aircraft site (upper panels) and their scatter diagrams (bottom panels) for (1) Amsterdam, (2) London, (3) Vancouver, (4) Paris, (5) Milan, and (6) Rome. Green and blue dots show the GOSAT XCO_2 data over land and ocean regions, respectively. Red dots and lines in the upper panels indicate the aircraft-based XCO_2 and fitted curves based on their data, respectively. Red and blue lines in the bottom panels denote the regression lines with statistical significance at the 95% level over land and ocean regions, respectively. The one-to-one lines are plotted as black lines.

(7) ICN (8) NRT (9) HND

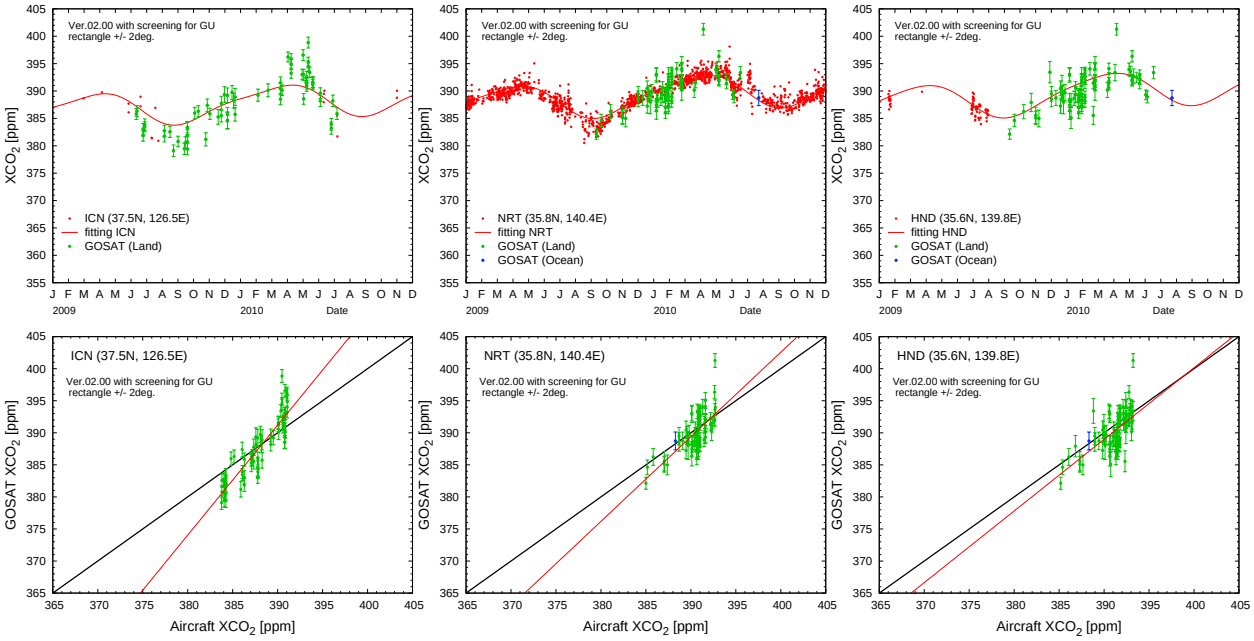

(10) NGO (11) KIX (12) DEL

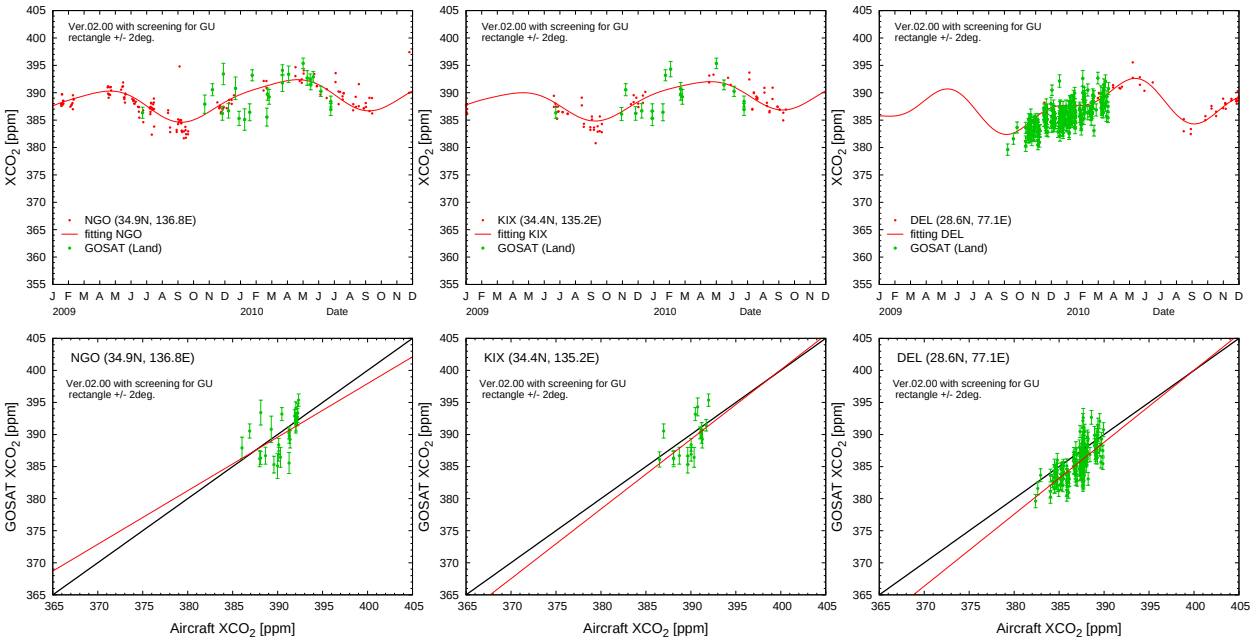

Fig. S- 4: Temporal variations of aircraft-based XCO_2 and GOSAT XCO_2 observed within $\pm 2^\circ$ latitude/longitude boxes centered at each aircraft site (upper panels) and their scatter diagrams (bottom panels) for (7) Incheon, (8) Narita, (9) Haneda, (10) Nagoya, (11) Kansai, and (12) Dehli. The others are the same as in Fig. S-3.

Fig. S- 5: Temporal variations of aircraft-based XCO_2 and GOSAT XCO_2 observed within $\pm 2°$ latitude/longitude boxes centered at each aircraft site (upper panels) and their scatter diagrams (bottom panels) for (13) Taipei, (14) Honolulu, (15) Manila, (16) Bangkok, (17) Guam, and (18) Singapore. The others are the same as in Fig. S-3.

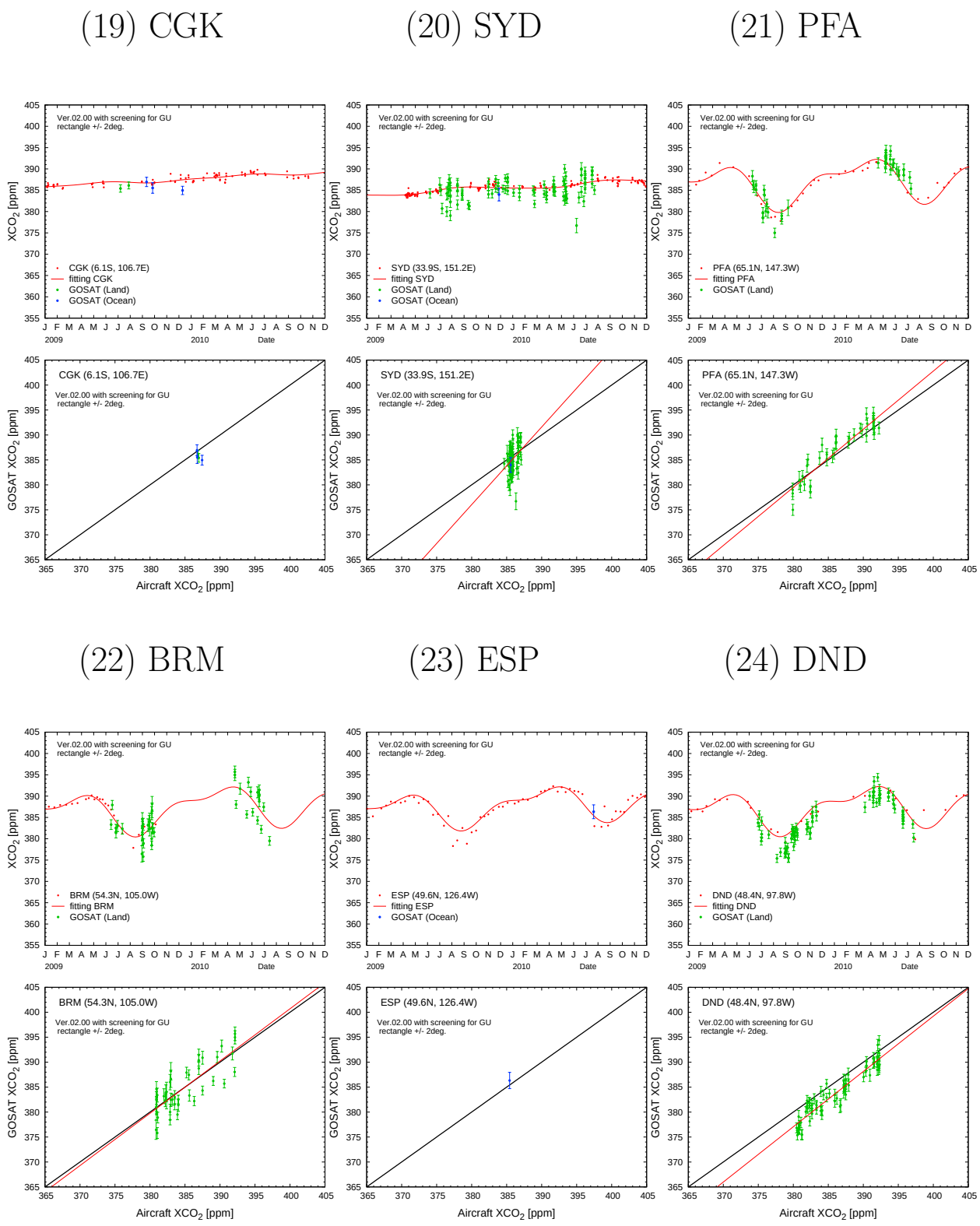

Fig. S- 6: Temporal variations of aircraft-based XCO_2 and GOSAT XCO_2 observed within $\pm 2°$ latitude/longitude boxes centered at each aircraft site (upper panels) and their scatter diagrams (bottom panels) for (19) Jakarta, (20) Sydney, (21) Poker Flat, (22) BERMS, (23) Estevan Point, and (24) Dahlen. The others are the same as in Fig. S-3.

(25) LEF (26) NHA (27) WBI

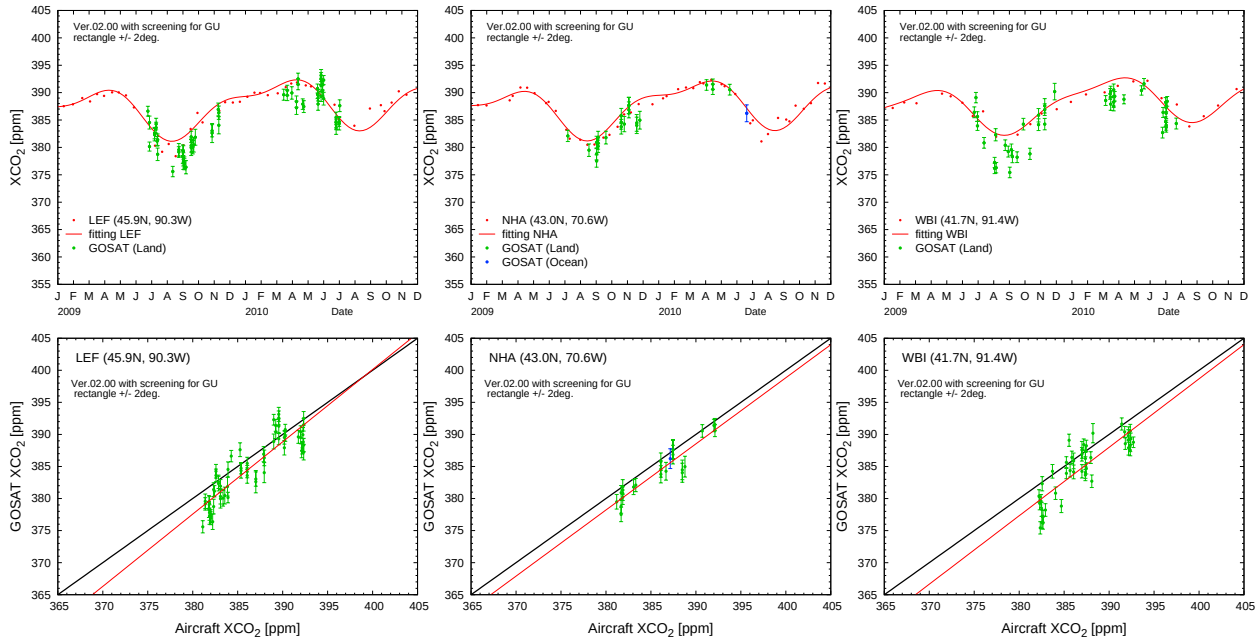

(28) THD (29) BNE (30) CAR

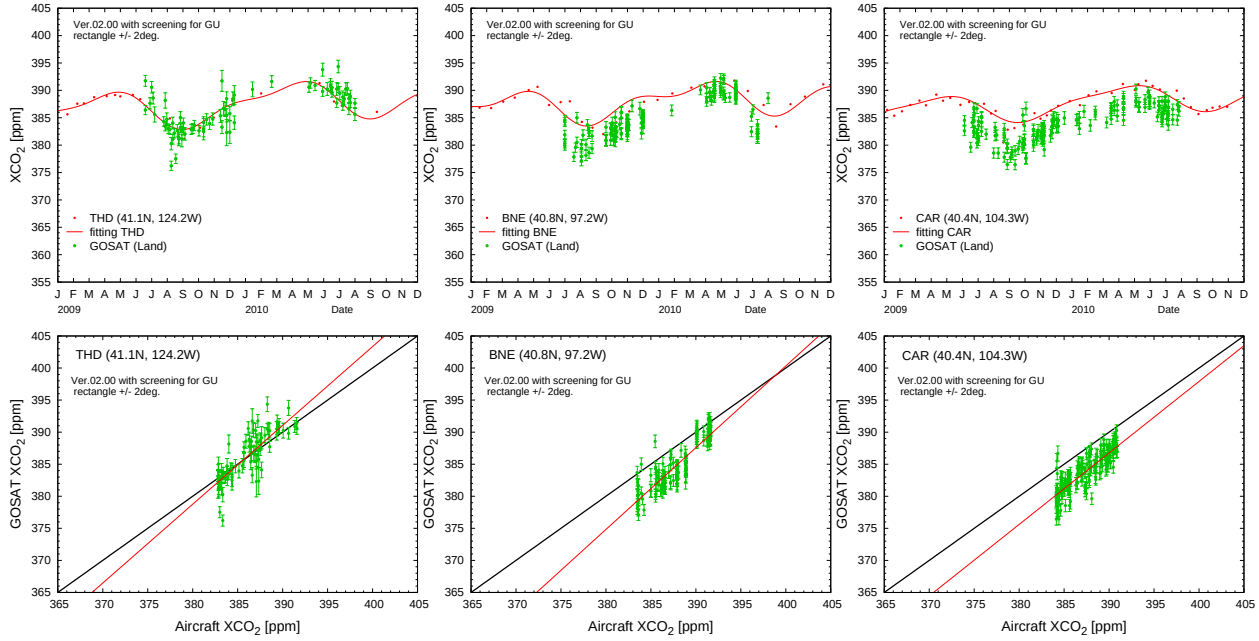

Fig. S- 7: Temporal variations of aircraft-based XCO_2 and GOSAT XCO_2 observed within $\pm 2^\circ$ latitude/longitude boxes centered at each aircraft site (upper panels) and their scatter diagrams (bottom panels) for (25) Park Falls, (26) Worcester, (27) West Branch, (28) Trinidad Head, (29) Beaver Crossing, and (30) Briggsdale. The others are the same as in Fig. S-3.

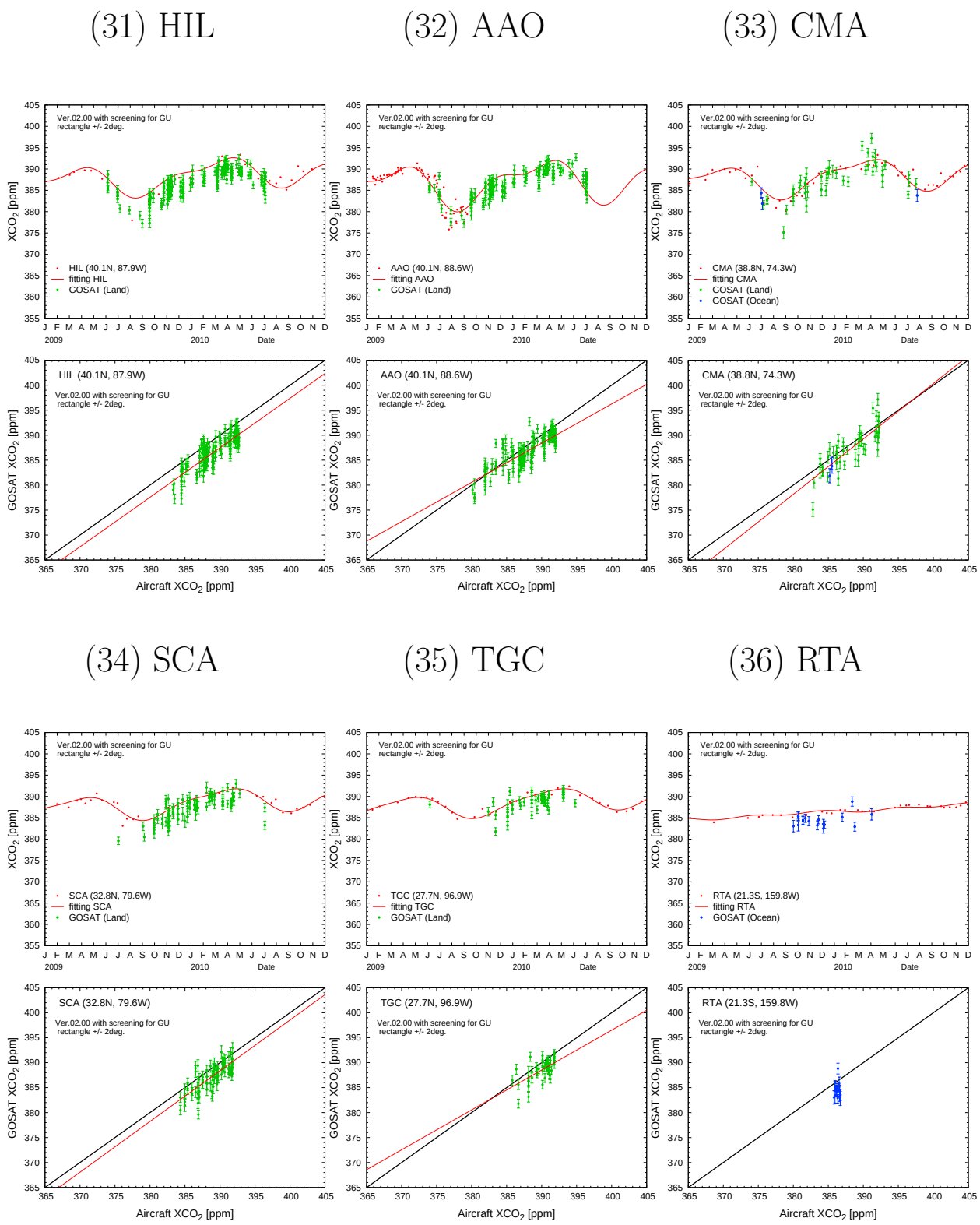

Fig. S- 8: Temporal variations of aircraft-based XCO_2 and GOSAT XCO_2 observed within $\pm 2°$ latitude/longitude boxes centered at each aircraft site (upper panels) and their scatter diagrams (bottom panels) for (31) Homer, (32) Bondville, (33) Cape May, (34) Charleston, (35) Sinton, and (36) Rarotonga. The others are the same as in Fig. S-3.

(37) SGP (38) YAK (39) SUR

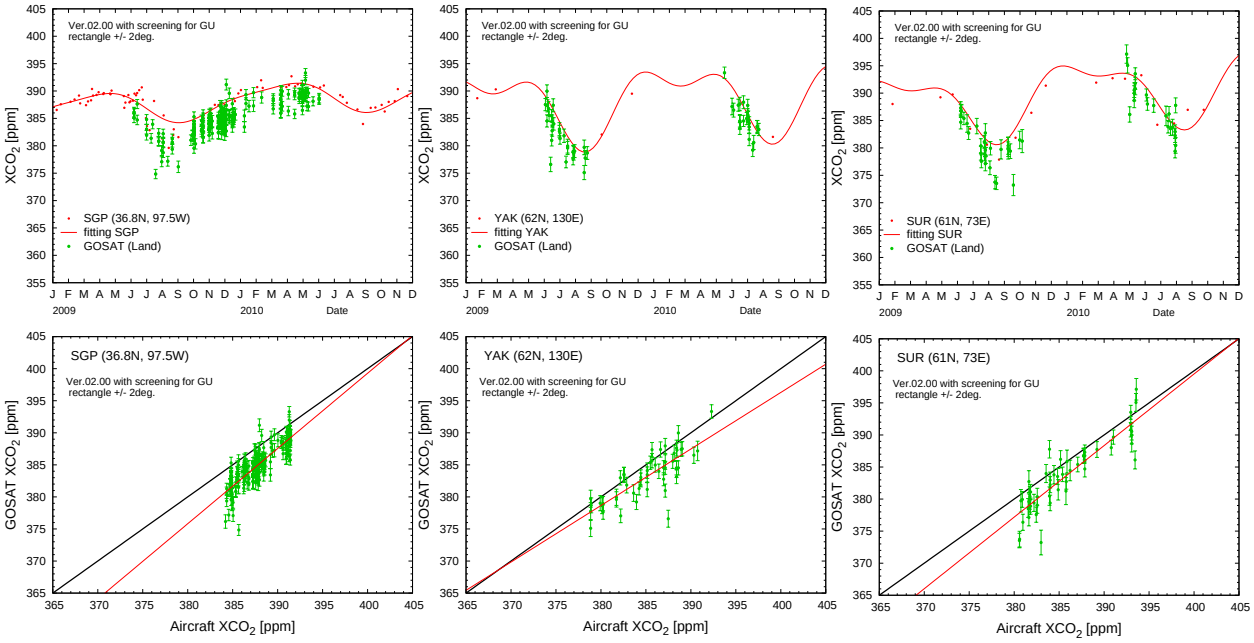

(40) NOV (41) SGM

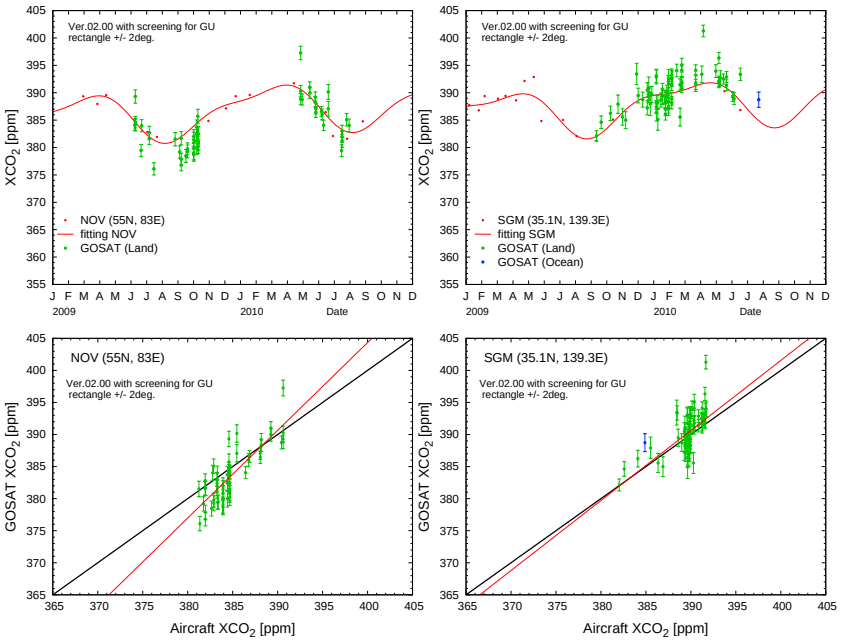

Fig. S- 9: Temporal variations of aircraft-based XCO_2 and GOSAT XCO_2 observed within $\pm 2°$ latitude/longitude boxes centered at each aircraft site (upper panels) and their scatter diagrams (bottom panels) for (37) the Southern Great Plains, (38) Yakutsk, (39) Surgut, (40) Novosibirsk, and (41) Sagami-bay. The others are the same as in Fig. S-3.

Fig. S- 10: Temporal variations of aircraft-based XCO_2 and GOSAT XCO_2 observed within $\pm 5^\circ$ latitude/longitude boxes centered at each aircraft site (upper panels) and their scatter diagrams (bottom panels) for (1) Amsterdam, (2) London, (3) Vancouver, (4) Paris, (5) Milan, and (6) Rome. The others are the same as in Fig. S-3.

(7) ICN (8) NRT (9) HND

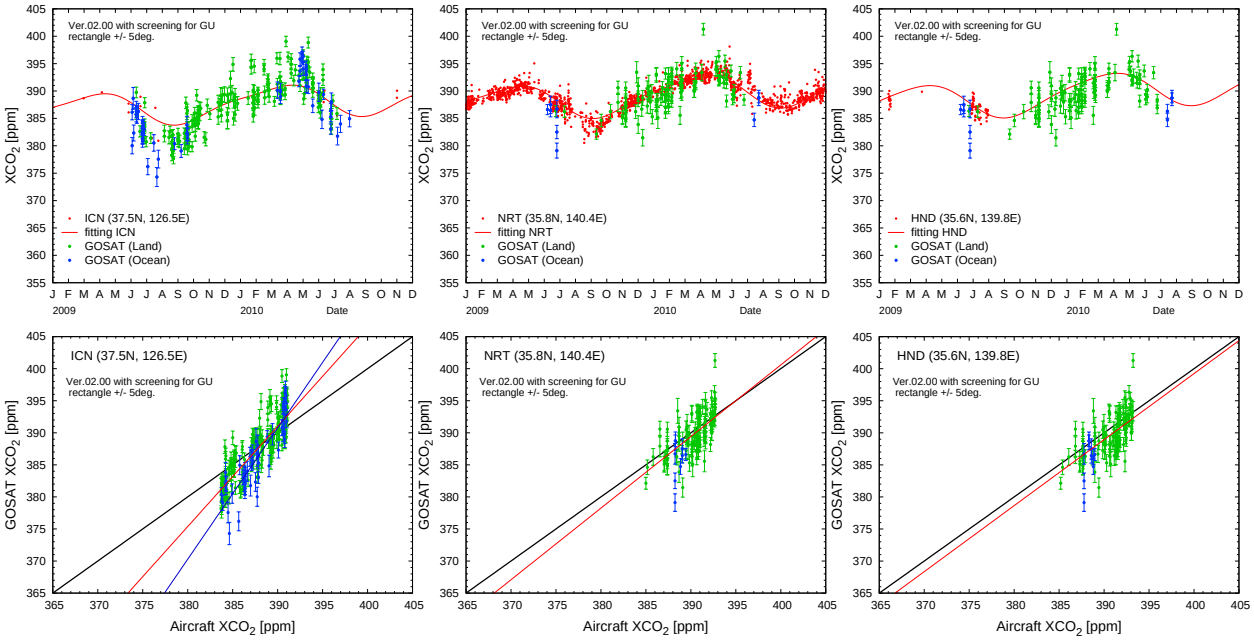

(10) NGO (11) KIX (12) DEL

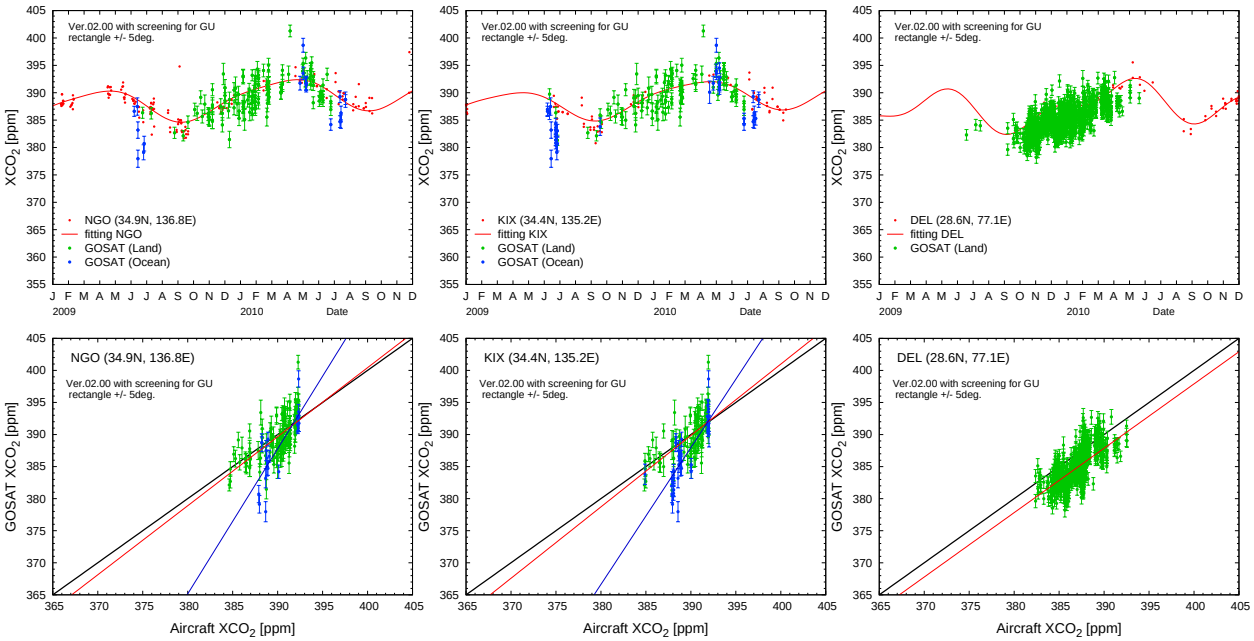

Fig. S- 11: Temporal variations of aircraft-based XCO_2 and GOSAT XCO_2 observed within $\pm 5^\circ$ latitude/longitude boxes centered at each aircraft site (upper panels) and their scatter diagrams (bottom panels) for (7) Incheon, (8) Narita, (9) Haneda, (10) Nagoya, (11) Kansai, and (12) Delhi. The others are the same as in Fig. S-3.

(13) TPE (14) HNL (15) MNL

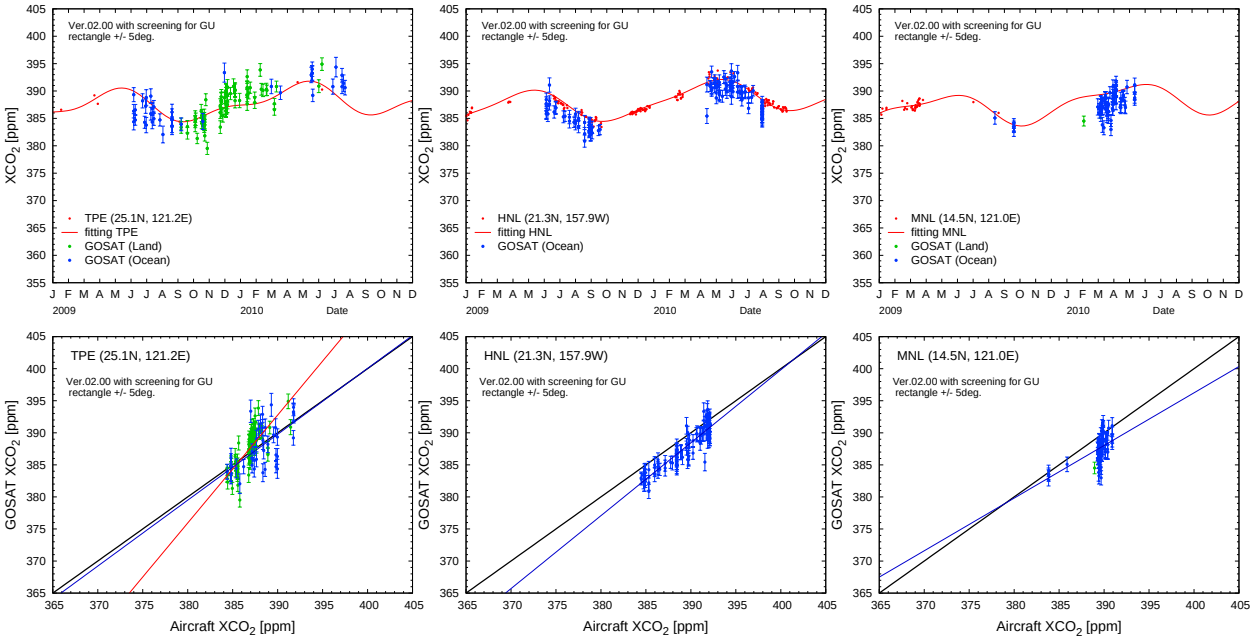

(16) BKK (17) GUM (18) SIN

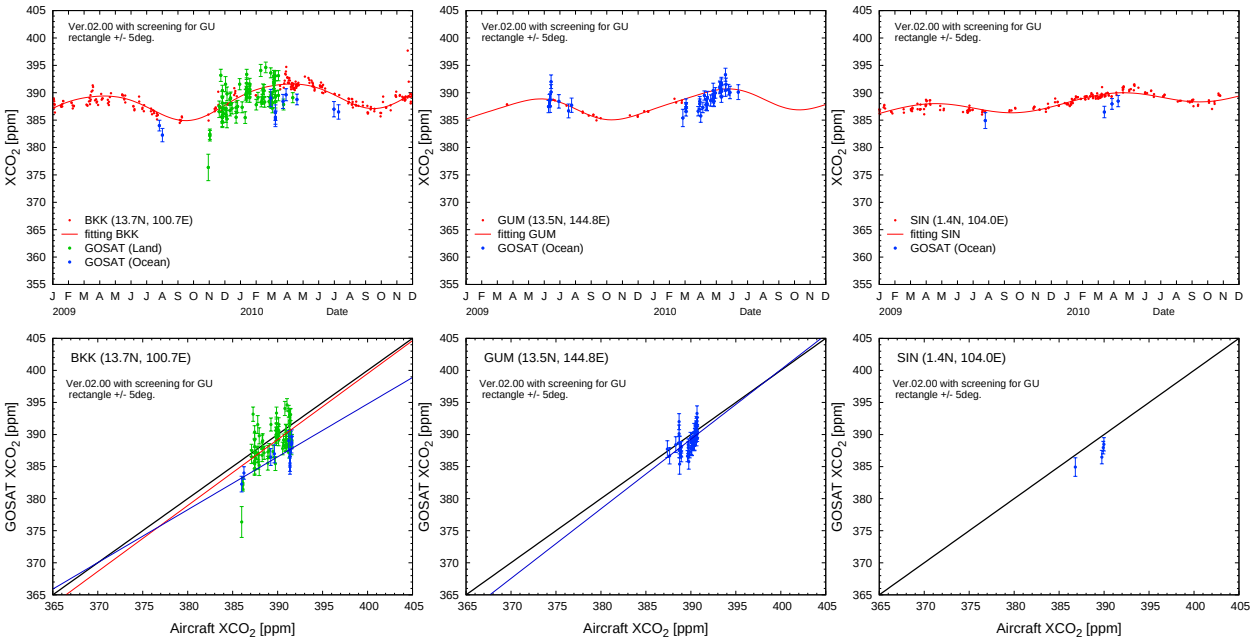

Fig. S- 12: Temporal variations of aircraft-based XCO_2 and GOSAT XCO_2 observed within $\pm 5^\circ$ latitude/longitude boxes centered at each aircraft site (upper panels) and their scatter diagrams (bottom panels) for (13) Taipei, (14) Honolulu, (15) Manila, (16) Bangkok, (17) Guam, and (18) Singapore. The others are the same as in Fig. S-3.

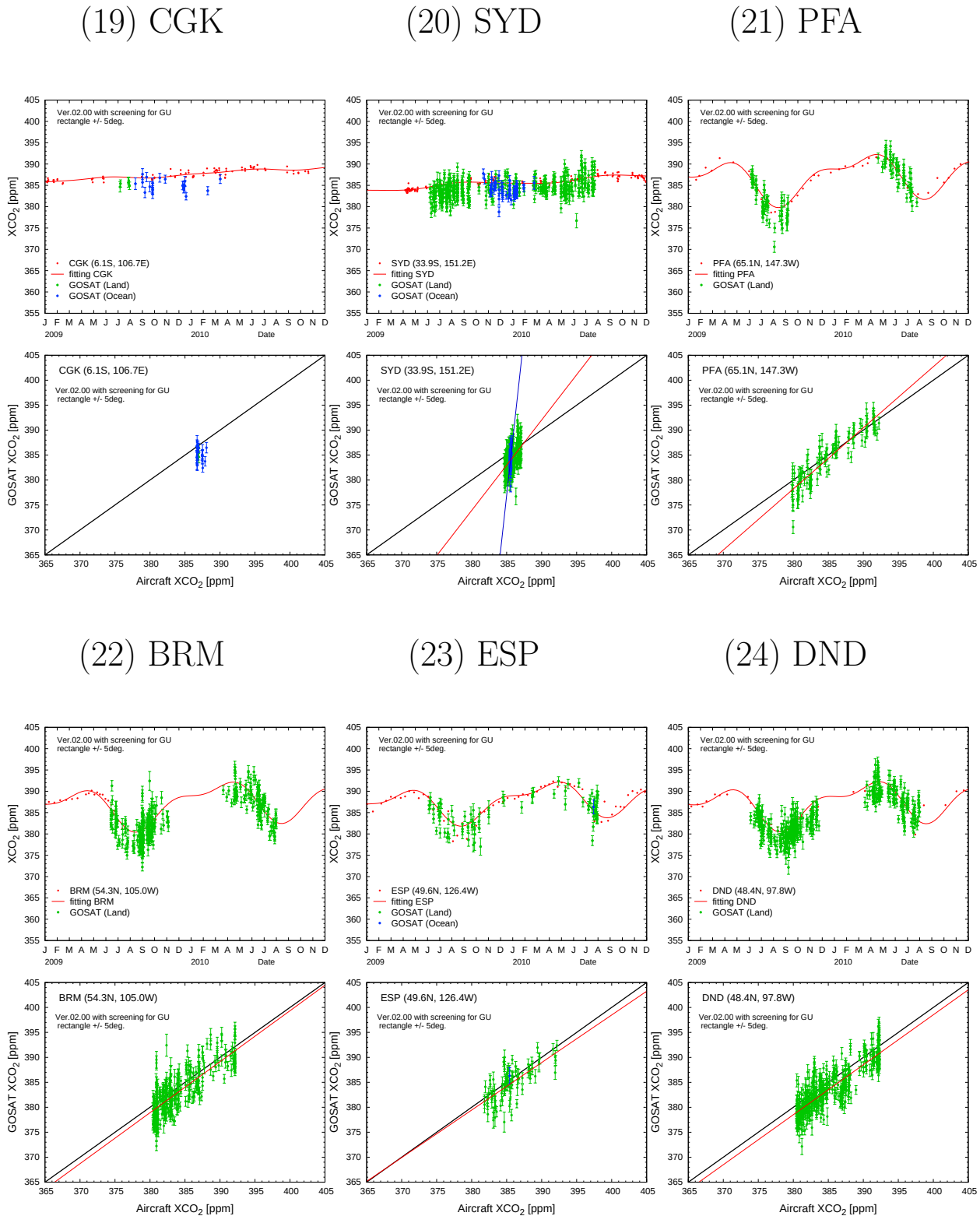

Fig. S- 13: Temporal variations of aircraft-based XCO_2 and GOSAT XCO_2 observed within $\pm 5°$ latitude/longitude boxes centered at each aircraft site (upper panels) and their scatter diagrams (bottom panels) for (19) Jakarta, (20) Sydney, (21) Poker Flat, (22) BERMS, (23) Estevan Point, and (24) Dahlen. The others are the same as in Fig. S-3.

(25) LEF (26) NHA (27) WBI

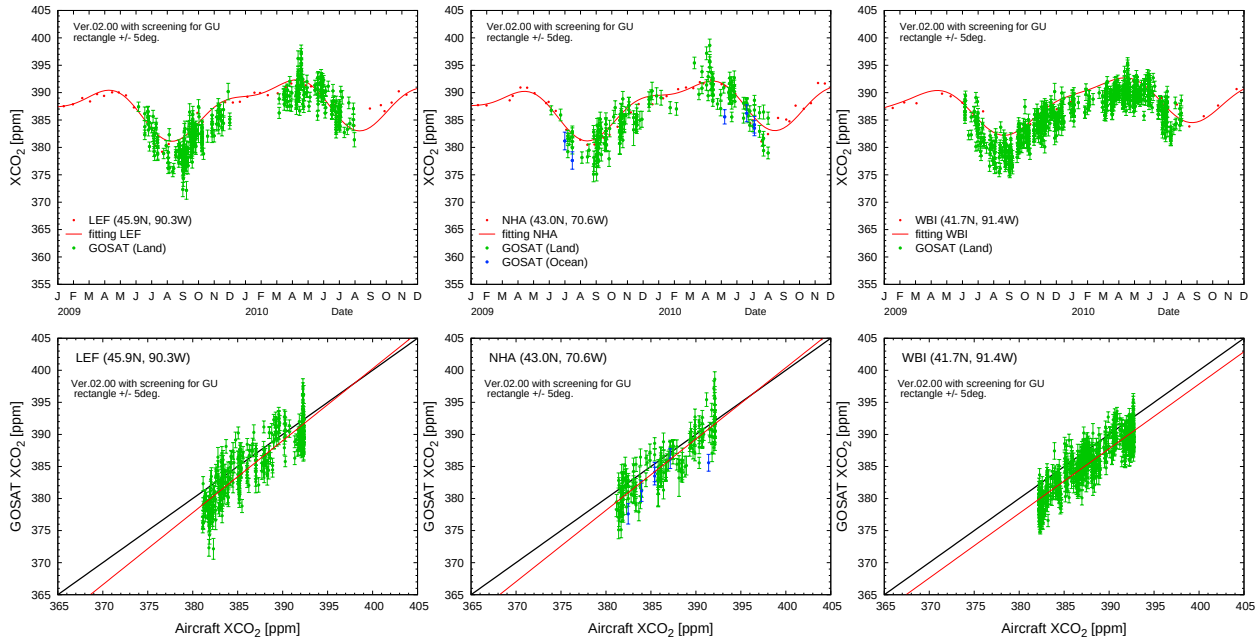

(28) THD (29) BNE (30) CAR

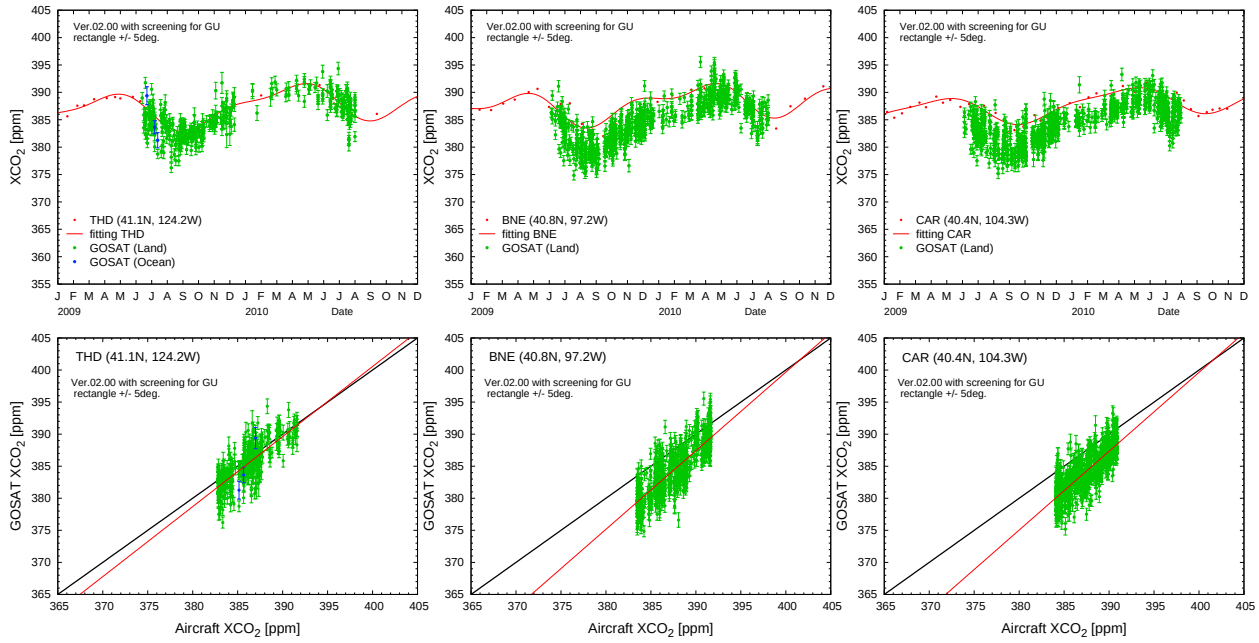

Fig. S- 14: Temporal variations of aircraft-based XCO_2 and GOSAT XCO_2 observed within $\pm 5^\circ$ latitude/longitude boxes centered at each aircraft site (upper panels) and their scatter diagrams (bottom panels) for (25) Park Falls, (26) Worcester, (27) West Branch, (28) Trinidad Head, (29) Beaver Crossing, and (30) Briggsdale. The others are the same as in Fig. S-3.

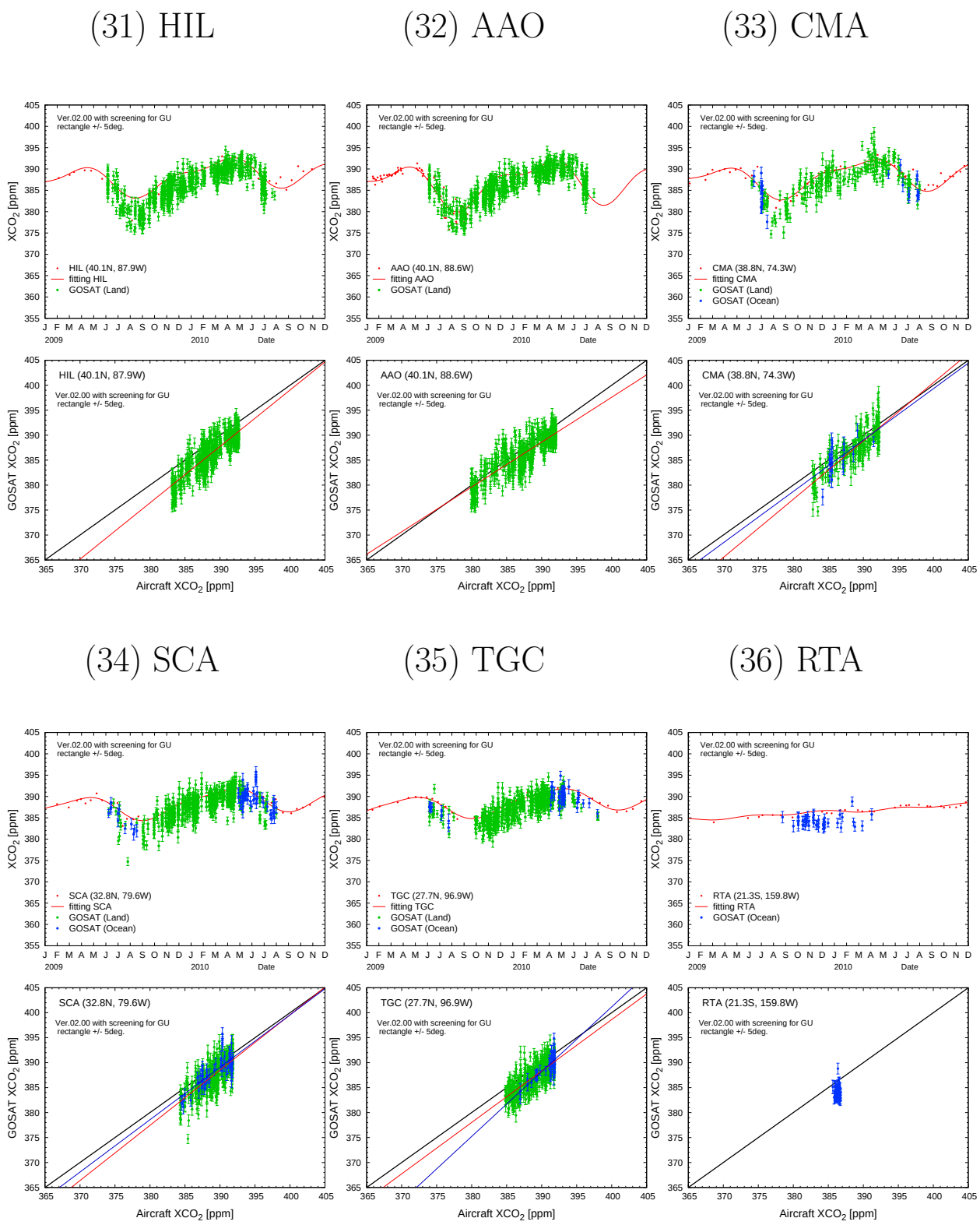

Fig. S- 15: Temporal variations of aircraft-based XCO_2 and GOSAT XCO_2 observed within $\pm 5^\circ$ latitude/longitude boxes centered at each aircraft site (upper panels) and their scatter diagrams (bottom panels) for (31) Homer, (32) Bondville, (33) Cape May, (34) Charleston, (35) Sinton, and (36) Rarotonga. The others are the same as in Fig. S-3.

(37) SGP (38) YAK (39) SUR

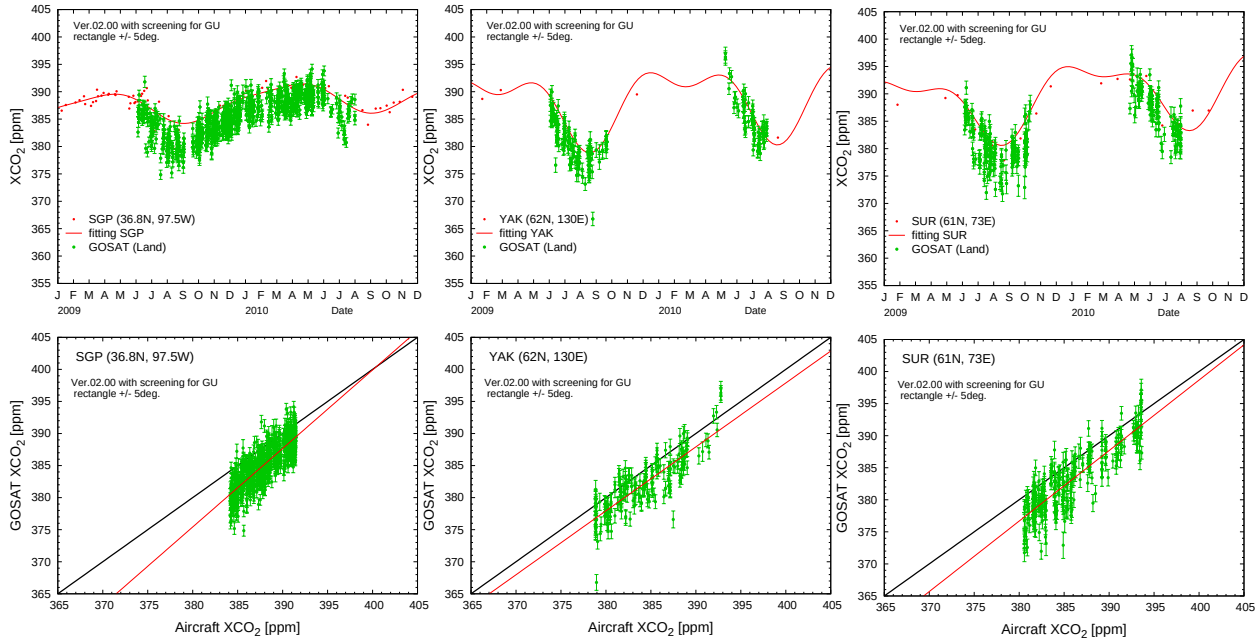

(40) NOV (41) SGM

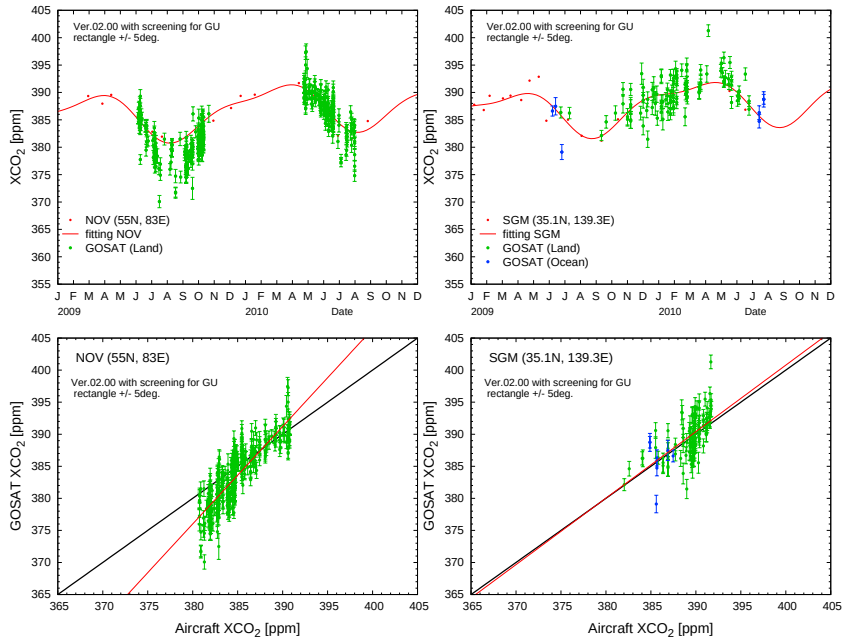

Fig. S- 16: Temporal variations of aircraft-based XCO_2 and GOSAT XCO_2 observed within $\pm 5^\circ$ latitude/longitude boxes centered at each aircraft site (upper panels) and their scatter diagrams (bottom panels) for (37) the Southern Great Plains, (38) Yakutsk, (39) Surgut, (40) Novosibirsk, and (41) Sagami-bay. The others are the same as in Fig. S-3.

(a)

±2 deg.

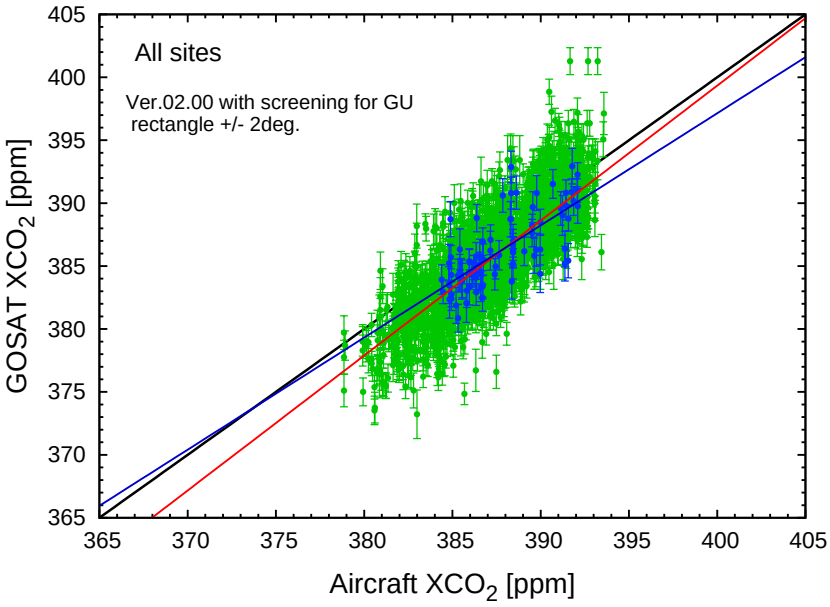

(b)

±5 deg.

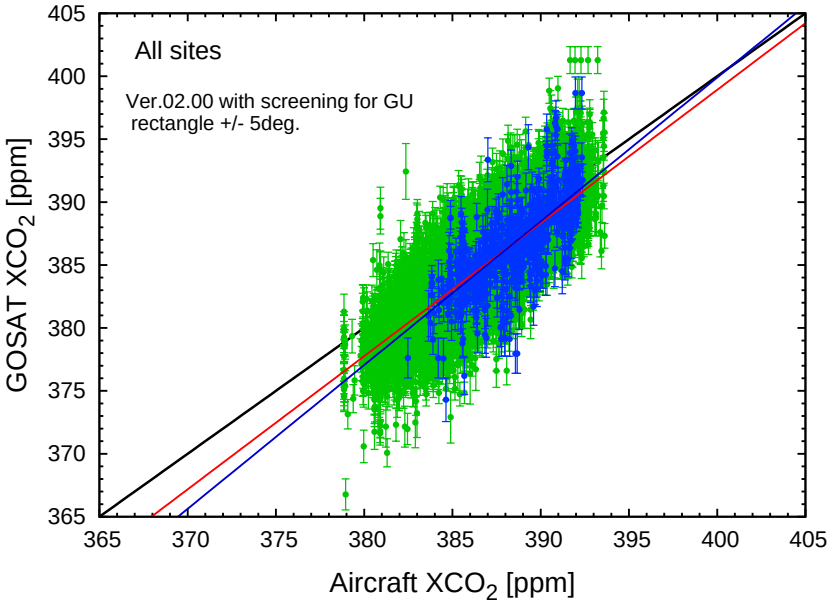

Fig. S- 17: Scatter diagrams between GOSAT XCO_2 observed within (a)±2°and (b)±5° latitude/longitude boxes centered at each aircraft observation site and the aircraft-based XCO_2 (estimate values obtained by a curve fitting method). Green and blue dots indicate XCO_2 obtained over land and ocean regions, respectively. Red and blue lines denote the regression lines with statistical significance at the 95% level over land and ocean regions, respectively. The one-to-one lines are plotted as black lines.